nature geoscience

ARTICLES

https://doi.org/10.1038/s41561-021-00759-4

Distinct sources of interannual subtropical and subpolar Atlantic overturning variability

Yavor Kostov[1]✉, Helen L. Johnson[2], David P. Marshall[3], Patrick Heimbach[4,5,6], Gael Forget[7], N. Penny Holliday[8], M. Susan Lozier[9], Feili Li[9], Helen R. Pillar[4] and Timothy Smith[4]

The Atlantic meridional overturning circulation (AMOC) is pivotal for regional and global climate due to its key role in the uptake and redistribution of heat and carbon. Establishing the causes of historical variability in AMOC strength on different timescales can tell us how the circulation may respond to natural and anthropogenic changes at the ocean surface. However, understanding observed AMOC variability is challenging because the circulation is influenced by multiple factors that co-vary and whose overlapping impacts persist for years. Here we reconstruct and unambiguously attribute intermonthly and interannual AMOC variability at two observational arrays to the recent history of surface wind stress, temperature and salinity. We use a state-of-the-art technique that computes space- and time-varying sensitivity patterns of the AMOC strength with respect to multiple surface properties from a numerical ocean circulation model constrained by observations. While, on interannual timescales, AMOC variability at 26° N is overwhelmingly dominated by a linear response to local wind stress, overturning variability at subpolar latitudes is generated by the combined effects of wind stress and surface buoyancy anomalies. Our analysis provides a quantitative attribution of subpolar AMOC variability to temperature, salinity and wind anomalies at the ocean surface.

Throughout the upper kilometre, the Atlantic meridional overturning circulation (AMOC) carries warm, high-salinity waters northward, while at depth it transports colder, low-salinity waters southward in a zonal mean sense[1]. Coupled climate models suggest that the AMOC is likely to weaken over the coming decades, resulting in a decrease in the associated northward heat transport, with widespread implications for regional and global climate[2]. Continuous observations of the AMOC since 2004 at 26° N, the location of the Rapid Climate Change–Meridional Overturning Circulation and Heatflux Array (RAPID–MOCHA), and since 2014 at subpolar latitudes, where the Overturning in the Subpolar North Atlantic Program (OSNAP) array has been deployed, reveal large-amplitude variability on all timescales accessible to date[3–5]. Disentangling the roles of anomalies in wind stress, sea surface temperature (SST) and sea surface salinity (SSS) in driving historical AMOC variability has been a major obstacle, limiting our understanding of past changes and our ability to critically assess model predictions of the future of the overturning circulation. The fact that SST and SSS themselves respond to changes in the ocean circulation, which can be independent of local atmospheric forcing, makes distinguishing cause and effect even more challenging.

Attributing AMOC variability has traditionally been approached through perturbation experiments in climate models[6,7]. However, a prohibitively large number of perturbation simulations is necessary to fully resolve the spatially and seasonally varying sensitivity of the AMOC to surface boundary conditions. Another standard method in attribution studies involves statistical analysis of the co-variability between the overturning circulation and surface properties such as air–sea heat flux, SST, SSS, and wind stress[7,8]. Still, many observables in the climate system co-vary, and correlations among them do not reveal the direction of causality. In this article, we take a different approach towards attribution and use the adjoint[9,10] of an ocean model to establish unambiguous causal relationships[11,12] between quantities at the air–sea interface and the lagged response of the AMOC. The adjoint of an ocean circulation model allows us to compute the sensitivity of a chosen metric, here the AMOC at a given latitude, to a range of variables, parameter choices, initial conditions and boundary conditions at various lead times[10–12]. We use algorithmic differentiation[13] to generate the adjoint (Methods) of the ECCO (Estimating the Circulation and Climate of the Ocean) version 4 (hereafter, ECCO) configuration[10,14] of the Massachusetts Institute of Technology general circulation model (MITgcm), a state-of-the-art ocean general circulation model[15]. ECCO is an ocean state estimate, a data assimilation product in which a model simulation has been fit to historical observations in a least-squares sense to best represent the evolution of ocean properties over the period 1992–2015[10,14,16,17]. ECCO skilfully reproduces measurements of temperature and salinity[10,14,16–18], as well as the overturning circulation in the North Atlantic (Supplementary Fig. 1).

In this article, we use this advanced computational framework to produce a quantitative attribution of AMOC variability in the subpolar North Atlantic to anomalies in SST, SSS and surface wind stress at different lead times. We focus on OSNAP-EAST rather than OSNAP-WEST (Fig. 1) because the observed mean transport and variability in the eastern subpolar North Atlantic is greater and is known to play an important role in the large-scale transformation from lighter into denser water masses[19–21]. We consider intermonthly and interannual timescales and contrast the response of the subpolar AMOC against that of the overturning across the RAPID–MOCHA mooring array at 26° N.

[1]Geography, University of Exeter, Exeter, UK. [2]Earth Sciences, University of Oxford, Oxford, UK. [3]Physics, University of Oxford, Oxford, UK. [4]Oden Institute for Computational Engineering and Sciences, University of Texas at Austin, Austin, TX, USA. [5]Jackson School of Geosciences, University of Texas at Austin, Austin, TX, USA. [6]Institute for Geophysics, University of Texas at Austin, Austin, TX, USA. [7]Earth, Atmospheric, and Planetary Sciences, Massachusetts Institute of Technology, Cambridge, MA, USA. [8]National Oceanography Centre, Southampton, UK. [9]Earth and Atmospheric Sciences, Georgia Institute of Technology, Atlanta, GA, USA. ✉e-mail: y.kostov@exeter.ac.uk

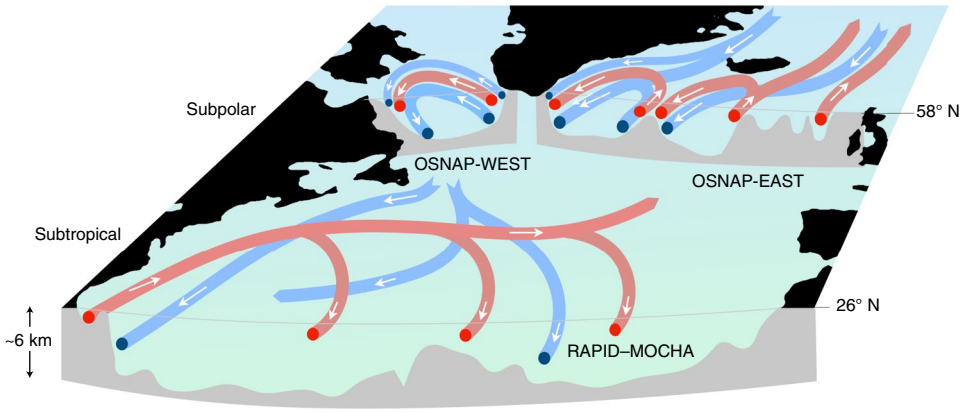

Fig. 1 | Schematic of the large-scale ocean circulation in the subtropical and subpolar North Atlantic. Colours differentiate major warm, saline (red) and cool, fresh (blue) pathways of ocean currents. Bathymetric cross sections are shown in grey at the locations of the OSNAP-WEST, OSNAP-EAST and RAPID–MOCHA arrays.

Reconstruction of the OSNAP-EAST and RAPID–MOCHA AMOC

We use the adjoint of the MITgcm ECCO configuration to isolate the sensitivity of the overturning circulation to wind stress from its sensitivity to SST and SSS. This separation is critical because changes in wind can lead to substantial anomalies in ocean temperature and salinity. We then convolve these sensitivity patterns ($\mathcal{G}_\mathcal{P}$), which depend on the season, with surface wind stress, SST and SSS anomalies between 1992 and 2015 from the ECCO state estimate. Each convolution provides an estimate for the time-evolving contribution C of the anomaly in a particular ocean surface property $\mathcal{P}$ (temperature, salinity or wind stress) to historical variability in the rate of meridional overturning (the volume transport in Sverdrups, where $1\,\mathrm{Sv} = 10^6\,\mathrm{m^3\,s^{-1}}$):

$$C_\mathcal{P}(t) = \int_{t-\tau}^{t}\int \mathcal{P}(\mathbf{x}, t')\mathcal{G}_\mathcal{P}(t;\mathbf{x}, t-t')\,\mathrm{d}\mathbf{x}\mathrm{d}t' \qquad (1)$$

where $\mathcal{P}$ is the surface property anomaly relative to the climatology at a lead time t', up to a memory τ and location $\mathbf{x}$; see Methods for further details. We sum the contributions from SST, SSS and wind stress anomalies relative to the seasonal mean and then add the climatological seasonal cycle in overturning[11] from the ECCO state estimate. We thus reconstruct AMOC variability relative to the long-term mean at the latitudes of both the OSNAP-EAST and the RAPID–MOCHA arrays. We separately consider how individual sources of variability contribute to the total reconstruction. Furthermore, we explore how the seasonality in wind stress contributes to variability in the overturning relative to the long-term mean.

The reconstructed overturning variability across OSNAP-EAST (Fig. 2a) is significantly correlated ($R = 0.69$, and $R = 0.72$ if we detrend the time series) with the historical overturning as represented in ECCO. The reconstruction of overturning variability at the latitude of the RAPID–MOCHA array (Fig. 2b), based on surface wind stress, SST and SSS, also shows good agreement with the ECCO state estimate ($R = 0.89$) and with the direct observational estimate ($R = 0.70$). Our reconstruction skilfully reproduces the sign, magnitude and timing of the AMOC anomalies (Fig. 2a,b). This high level of agreement suggests that AMOC variability is dominated by processes and mechanisms that our analysis largely captures.

The OSNAP-EAST observational record of 21 months is much shorter than that in the subtropical Atlantic, but first indications suggest that our reconstruction also captures some of the observed AMOC variability here. We interpolate our OSNAP-EAST reconstruction onto the same 30-day time windows as the direct observational estimate (Extended Data Fig. 1). In 14 out of the 15 time windows where OSNAP-EAST observations and model output are both available, our envelope of reconstructions overlaps with the direct observational estimate within one standard error (Extended Data Fig. 1). However, over this short record, intermonthly variability in our reconstructed OSNAP-EAST overturning is not positively or significantly correlated with the observational time series.

Nonlinearity in the sensitivity of the overturning circulation to surface forcing such as SST and SSS is a key potential source of uncertainty in our reconstructions. An important manifestation of nonlinearity in the overturning is the dependence of the sensitivity patterns, and hence the AMOC reconstructions, on the evolving background state of the ocean. For example, the exact sites of intense winter convection and deep-water formation in the North Atlantic differ from one year to another. The grey-shaded envelopes in Fig. 2a,b show the spread in reconstructed AMOC variability that results from using sensitivity patterns computed over two different historical periods in ECCO: one ending in 2001–2002 and one in 2006–2007 (Methods). This largely reflects changes in the sensitivity to winter surface buoyancy anomalies between the two periods analysed. This can be seen by comparing the large spread in the full reconstruction that includes the buoyancy component (Fig. 2a) with the diminished spread in the wind-only reconstruction (Fig. 2c). The dependence on the background state is more pronounced in the OSNAP-EAST time series than in the subtropical RAPID–MOCHA AMOC and explains the lower skill in recovering the subpolar overturning. In addition, for numerical reasons, the adjoint of the model approximates the parameterization of vertical mixing and sea-ice physics, nonlinear processes that are very active in the high-latitude oceans and thus affect more strongly the OSNAP-EAST reconstruction compared with the RAPID–MOCHA AMOC.

Attribution of AMOC variability to wind, SST and SSS

Much of the variability ($R = 0.94$) in historical overturning at 26° N can be explained in terms of wind-driven circulation anomalies (Figs. 2d and 4a,b[11]). A large fraction of the intermonthly AMOC anomalies at the RAPID–MOCHA array is attributed to processes within the surface Ekman boundary layer ($R = 0.70$, Extended Data Fig. 2), where there is a local balance between wind stress and a component of the Coriolis force[22]. Surface buoyancy anomalies contribute to low-frequency variability in the subtropical AMOC, such as the reconstructed 2007–2011 decline in the overturning at the RAPID–MOCHA array (Fig. 3b). This historical weakening of the AMOC is very pronounced in the observational time series[4] (Fig. 2b)

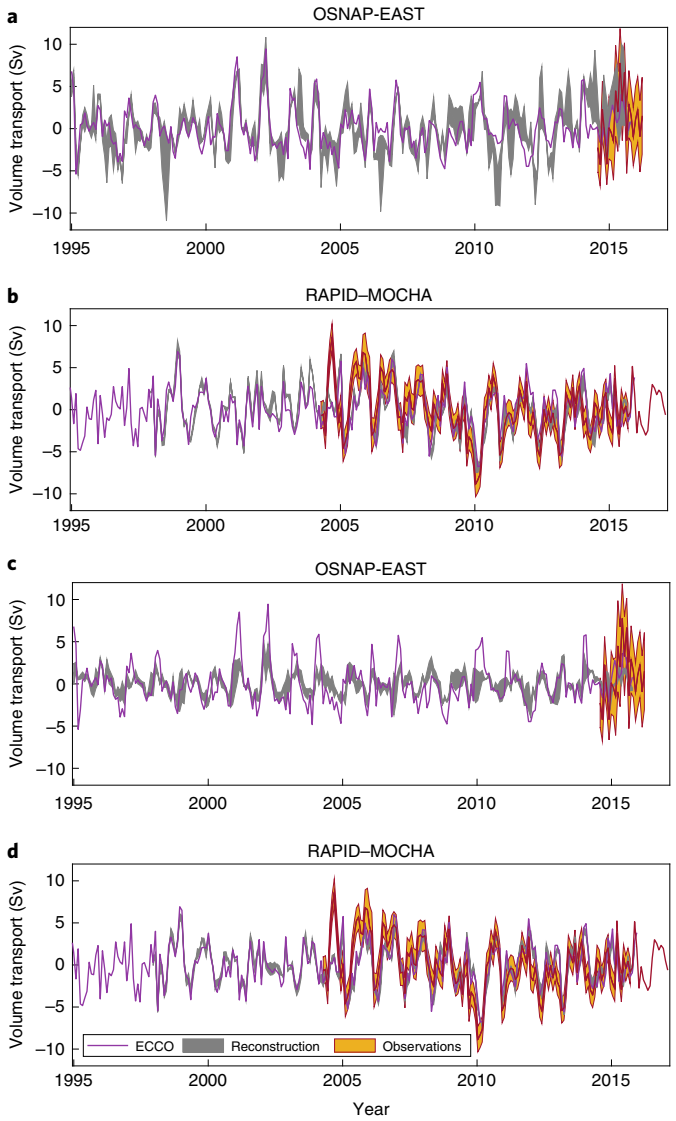

Fig. 2 | Reconstruction of overturning in the North Atlantic. a–d, Linear reconstruction (grey) of variability in OSNAP-EAST (**a**,**c**) and RAPID-MOCHA (**b**,**d**) meridional overturning (volume transport in Sv) compared with the ECCO state estimate (purple) and the direct observational estimate (yellow and brown). Anomalies are shown relative to the long-term mean. The yellow shaded envelopes indicate ±1 standard deviation of the observational uncertainty at OSNAP-EAST (see ref. [19]) and RAPID-MOCHA (see ref. [35]), and the thick brown lines show the mean estimates. The uncertainty of the observed RAPID-MOCHA overturning is not available for the last 17 months of the time series (the thick brown line in **b** and **d**). The reconstructions in **a** and **b** include contributions due to surface wind stress, SST and SSS as well as the climatological seasonal cycle in overturning from ECCO. The thickness of the grey shading in **a** and **b** indicates the spread between two estimates of the reconstructed AMOC in ECCO, reflecting variability in the reference state about which the linearized reconstruction is computed (Methods). The reconstructions in **c** and **d** show only contributions due to surface wind stress anomalies—including the contribution from the seasonal cycle in winds—under fixed SST and SSS.

but less so in ECCO (Fig. 2b), possibly because high-latitude density variability in the state estimate is biased relative to observations[23].

Wind-induced variability, including the seasonal cycle in surface wind stress, also contributes noticeably to anomalies in the overturning across OSNAP-EAST ($R=0.68$, Fig. 2c). However, winds do not overwhelmingly dominate the subpolar AMOC as they do at 26° N. If we consider only wind stress anomalies relative to the seasonal cycle, they explain 31% of the variability at OSNAP-EAST ($R=0.56$). Anomalies in SST and SSS relative to the seasonal cycle jointly explain a smaller but comparable fraction, 12% of variability ($R=0.35$) in the OSNAP-EAST AMOC as represented in ECCO. SST and SSS anomalies drive interannual variability in the OSNAP-EAST circulation that is similar in magnitude to the large background seasonal cycle in overturning (Fig. 3a). All of these components—due to wind stress, SST and SSS—combine to generate variability at the OSNAP-EAST array that can be explained largely by a geostrophic balance between the Coriolis force and pressure gradients even on intermonthly timescales (Extended Data Fig. 3). We note that this is in contrast to variability at the RAPID–MOCHA line, where geostrophic balance dominates only at low frequencies[4,24,25] (Extended Data Fig. 3).

At both subtropical and subpolar latitudes, SSS-induced AMOC variability is significantly anti-correlated with SST-induced AMOC variability (Fig. 3). To explore this relationship, we consider the AMOC sensitivity to surface boundary conditions in particular periods of the ECCO state estimate (Methods). The estimated SST and SSS contributions to OSNAP-EAST variability shown in Fig. 3a are anti-correlated with $R=-0.42$. This statistical relationship indicates a partial compensation between the SSS- and SST-driven contributions to historical AMOC changes. Generally, the variability due to SSS dominates over that due to SST at OSNAP-EAST (Fig. 3a), while at 26° N this is not the case (Fig. 3b).

Spatial origins of AMOC variability

Figure 4 shows the spatial origins of the AMOC variability that results from anomalies in zonal wind stress, meridional wind stress, SST and SSS. Plotted is the root-mean-square contribution per unit area (Sv m^{-2}) to the convolutions in equation (1) over the period 1992–2015:

$$C_{\mathcal{P}}(\mathbf{x}) = \frac{1}{A(\mathbf{x})}\sqrt{\frac{1}{(T_f\cdot\tau)}\sum_{t=0}^{T_f}\sum_{t'=\max(t-\tau,0)}^{t}\left[\mathcal{P}\left(\mathbf{x},t'\right)\mathcal{G}_{\mathcal{P}}\left(t;\mathbf{x},t-t'\right)\right]^2} \quad (2)$$

where $A(\mathbf{x})$ is the horizontal surface area of the model grid cell in location $\mathbf{x}$, $\mathcal{P}$ represents the surface field anomalies relative to the climatology at a lead time t' summed up to a finite maximum memory τ. The function $\mathcal{G}_{\mathcal{P}}$ is the corresponding sensitivity pattern that depends on the season, the lead time t' and the geographical location $\mathbf{x}$ as in equation (1). We sum the convolution of $\mathcal{P}$ and $\mathcal{G}_{\mathcal{P}}$ until the end of the available time series $t=T_f$ and compute the root mean square (Methods). In effect, the convolution in equation (2) allows us to identify the regions where variability in wind stress, SST and SSS most strongly projects onto the corresponding AMOC sensitivity patterns and activates them (Fig. 4).

Local winds dominate AMOC variability at 26° N[11] via two mechanisms: (1) winds generate meridional transport anomalies within the Ekman surface boundary layer;[22] and (2) wind stress induces Rossby wave undulations of the thermocline that propagate westward and cause density anomalies along the western boundary of the Atlantic[24]. This build-up of density anomalies alters the balance between east-west pressure gradients in the ocean and the Coriolis force, thus changing the meridional transport[22] across the RAPID–MOCHA array. Remote winds play a larger role in generating variability in the overturning across OSNAP-EAST. For example, wind-driven coastal waves propagating along the boundaries transmit the impact of variability in subtropical and subarctic wind stress to the subpolar North Atlantic (Fig. 4f). These waves give rise

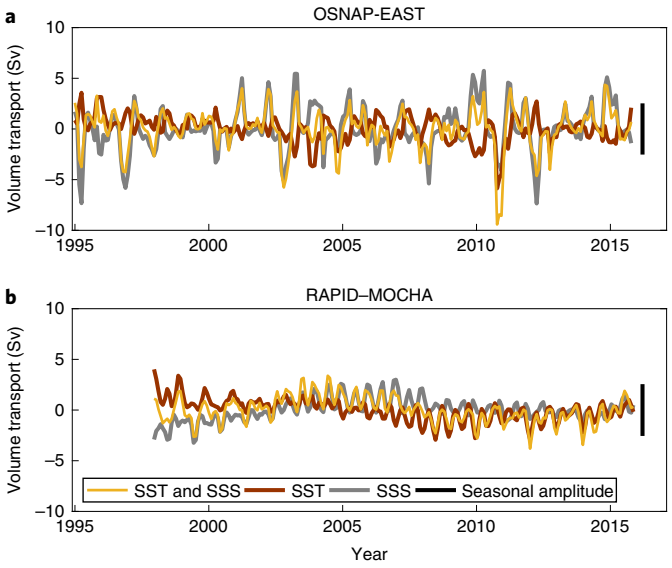

Fig. 3 | Contributions of SSS and SST to variability in overturning. **a**,**b**, SSS (grey) and SST (brown) contributions to the total buoyancy component (yellow) of the OSNAP-EAST (**a**) and RAPID-AMOC (**b**) reconstructions. The estimates use sets of sensitivity patterns based on a linearization of the model over a single historical period (Methods) while the full reconstructions in Fig. 2 use linearization over two historical periods to estimate uncertainty. For comparison, vertical black bars indicate the amplitude of the seasonal cycle in RAPID and OSNAP-EAST overturning in ECCO. The time series of contributions to RAPID–MOCHA overturning begin in 1998 because a 6-yr memory of SST and SSS is required (Methods), and the observationally constrained state estimate begins in 1992.

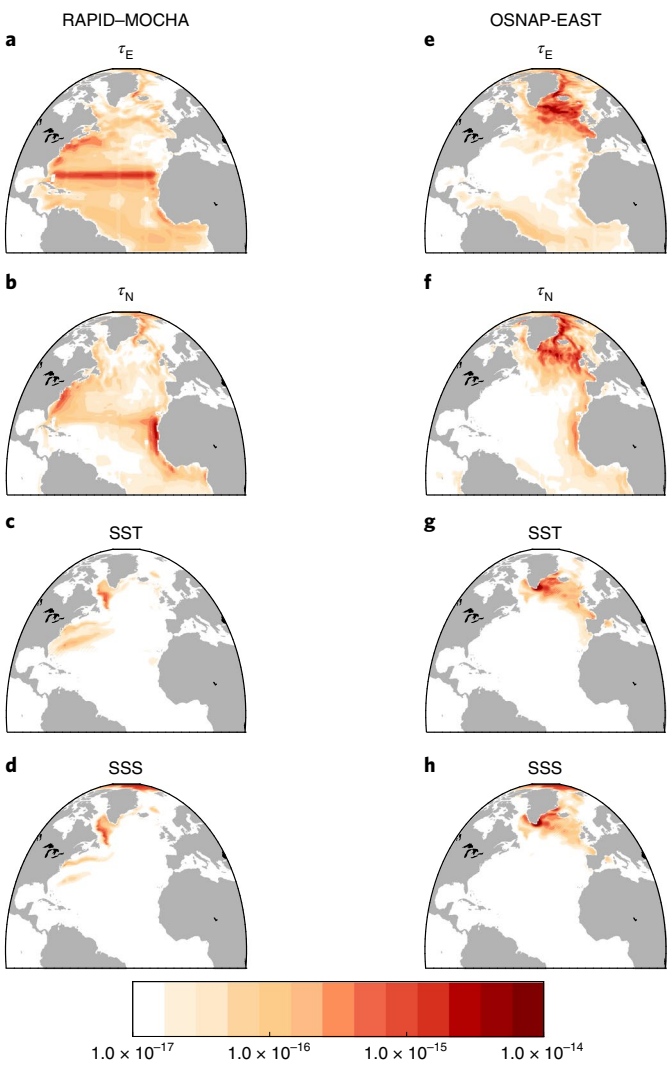

Fig. 4 | Spatial origins of variability in overturning at the RAPID–MOCHA and OSNAP-EAST arrays. a–d, RAPID–MOCHA array. **e–h**, OSNAP-EAST array. Colour indicates the root-mean-square contribution per unit area ($Sv\ m^{-2}$) to the convolutions in equation (1) over the period 1992–2015 using sensitivity patterns based on a linearization of the model over a historical period (Methods). Contributions due to zonal (**a**,**e**) and meridional (**b**,**f**) wind stress, SST (**c**,**g**) and SSS (**d**,**h**) are relative to the seasonal cycle. The scale is logarithmic.

to density anomalies on the Scottish and Greenland shelves and hence affect the balance between ocean pressure gradients along the OSNAP-EAST array and the Coriolis force. As a result, transport across the array changes. A similar wave-guide mechanism along the Atlantic's eastern boundary has also been identified in studies exploring the sensitivity of Labrador Sea heat content[26], heat transport across the Iceland–Scotland Ridge[27] and bottom pressure in the Arctic[28] to surface boundary conditions.

The overturning at OSNAP-EAST is also strongly influenced by local SSS and SST anomalies along the eastern coast of Greenland (Fig. 4g,h). This reflects two factors: (a) the existence of large thermohaline variability in the region and (b) the impact of density anomalies at the boundary on the balance between ocean pressure gradients and the Coriolis force. Note, however, that SST and SSS anomalies at these locations may be set by air–sea fluxes of heat and freshwater over a much larger geographical area and over a period of several years (Extended Data Fig. 4).

The buoyancy-forced component of the AMOC at 26° N exhibits long-term variability that arises from non-local surface buoyancy anomalies, namely, those in the Arctic and the Labrador Sea (Fig. 4c,d). Previous studies have suggested that deep convection in the Labrador Sea is related to subtropical AMOC variability on interannual and longer timescales[29,30]. We note that in the ECCO state estimate, there is deep convection both near the western boundary and in the interior of the Labrador Sea. However, the largest contribution of subpolar SST and SSS anomalies to reconstructed variability in RAPID–MOCHA overturning is concentrated in a narrow region near the western boundary of the subpolar basin (Fig. 4c,d and Extended Data Fig. 5). This region is known to play a key role in the ventilation of deep-water masses in the Labrador Sea[31]. By contrast, surface buoyancy anomalies in the convective interior of the Labrador Sea make a smaller contribution to variability at RAPID–MOCHA. This result demonstrates that the causal connection between water mass transformation in the Labrador Sea and the subtropical AMOC is complex. As previously suggested[19], the background ocean circulation can advect density anomalies from the Labrador Sea towards the eastern subpolar gyre where they imprint[32] on Lower North Atlantic Deep Water, the densest water mass in the AMOC lower limb. Anomalies in the volume and density of the Lower North Atlantic Deep Water layer can then be communicated to the subtropics at depth along the North Atlantic western boundary, and via ocean interior pathways, reaching 26° N on a timescale of approximately 4 years[33].

Implications for understanding future AMOC changes

Our analysis has shown that a large fraction of the observed and simulated variability in the Atlantic overturning circulation across the OSNAP-EAST array in the subpolar gyre, and across the RAPID–MOCHA array at 26° N, can be reconstructed using best

estimates of historical SST, SSS and wind anomalies convolved with AMOC sensitivity patterns computed from the adjoint of an ocean circulation model. This allows us to unambiguously attribute recent historical changes to particular sources of variability. At 26° N, the impact of remote (subpolar) surface buoyancy anomalies emerges only on decadal timescales (Fig. 3b). On shorter timescales, almost all of the variability in overturning can be reconstructed from knowledge of the past wind forcing alone[11] (Fig. 2d). However, our analysis suggests that reconstructing and predicting the overturning at the latitude of the OSNAP-EAST array presents a greater challenge because wind stress and surface buoyancy anomalies each explain a comparable fraction of the total variability in the subpolar circulation on interannual to decadal timescales. This provides strong motivation for continued observation of the AMOC by the OSNAP array to monitor and understand the state of the overturning circulation in that region and ultimately detect any anthropogenic influence.

Our results also confirm that sustained observation of SST and SSS anomalies in the subpolar North Atlantic, for example along the OSNAP-WEST line (Figs. 1 and 4c,d), may give us predictability for the buoyancy-induced decadal trend in the subtropical AMOC at the RAPID–MOCHA array. However, our reconstruction suggests that, compared with the subtropics, the overturning circulation in the subpolar North Atlantic is more sensitive to changes in the background ocean state (Fig. 2, compare the size of the shaded grey envelope of uncertainty in **a** and **b**) such as shifts in the sites of deep convection. This implies that future climate change may alter the interannual variability in the OSNAP-EAST overturning as well as its response to local and remote surface buoyancy anomalies. Attributing, understanding and predicting changes in AMOC transport at both subpolar and subtropical latitudes, therefore, hinges on the continued observation of the overturning[3–5] and of the background ocean state[34] as part of a coordinated Atlantic observation system.

Online content

Any methods, additional references, Nature Research reporting summaries, source data, extended data, supplementary information, acknowledgements, peer review information; details of author contributions and competing interests; and statements of data and code availability are available at https://doi.org/10.1038/s41561-021-00759-4.

Received: 8 February 2020; Accepted: 23 April 2021;
Published online: 31 May 2021

References

1. Lozier, M. S. Overturning in the North Atlantic. *Annu. Rev. Mar. Sci.* **4**, 291–315 (2012).
2. Stolpe, M. B., Medhaug, I., Sedláček, J. & Knutti, R. Multidecadal variability in global surface temperatures related to the Atlantic meridional overturning circulation. *J. Clim.* https://doi.org/10.1175/JCLI-D-17-0444.1 (2018).
3. Cunningham, S. A. et al. Temporal variability of the Atlantic meridional overturning circulation at 26.5° N. *Science* **317**, 935–938 (2007).
4. Smeed, D. A. et al. The North Atlantic Ocean is in a state of reduced overturning. *Geophys. Res. Lett.* **45**, 1527–1533 (2018).
5. Lozier, M. S. et al. Overturning in the Subpolar North Atlantic Program: a new international ocean observing system. *Bull. Am. Meteorol. Soc.* **98**, 737–752 (2017).
6. Biastoch, A., Böning, C. W., Getzlaff, J., Molines, J.-M. & Madec, G. Causes of interannual–decadal variability in the meridional overturning circulation of the North Atlantic Ocean. *J. Clim.* **21**, 6599–66615 (2008).
7. Polo, I., Robson, J., Sutton, R. & Balmaseda, M. A. The importance of wind and buoyancy forcing for the boundary density variations and the geostrophic component of the AMOC at 26° N. *J. Phys. Oceanogr.* **44**, 2387–2408 (2014).
8. Ortega, P. et al. Mechanisms of decadal variability in the Labrador Sea and the wider North Atlantic in a high-resolution climate model. *Clim. Dyn.* **49**, 2625–2647 (2017).
9. Errico, R. M. What is an adjoint model? *Bull. Am. Meteorol. Soc.* **78**, 2577–2591 (1997).
10. Forget, G. et al. ECCO version 4: an integrated framework for non-linear inverse modeling and global ocean state estimation. *Geosci. Model Dev.* **8**, 3071–3104 (2015).
11. Pillar, H., Heimbach, P., Johnson, H. & Marshall, D. Dynamical attribution of recent variability in Atlantic overturning. *J. Clim.* **29**, 3339–3352 (2016).
12. Smith, T. & Heimbach, P. Atmospheric origins of variability in the South Atlantic meridional overturning circulation. *J. Clim.* **32**, 1483–1500 (2019).
13. Giering, R. *Transformation of Algorithms in Fortran Version 1.15 (TAF Version 1.9.70)* (FastOpt, 2010).
14. Fukumori, I. et al. ECCO Version 4 Release 3 (NASA-JPL, 2017).
15. Marshall, J., Hill, C., Perelman, L. & Adcroft, A. Hydrostatic, quasi-hydrostatic, and nonhydrostatic ocean modeling. *J. Geophys. Res.* **102**, 5733–5752 (1997).
16. Forget, G., Ferreira, D. & Liang, X. On the observability of turbulent transport rates by Argo: supporting evidence from an inversion experiment. *Ocean Sci.* **11**, 839–853 (2015).
17. Fukumori, I., Heimbach, P., Ponte, R. M. & Wunsch, C. A dynamically consistent, multivariable ocean climatology. *Bull. Am. Meteorol. Soc.* **99**, 2107–2128 (2018).
18. Jackson, L. C. et al. The mean state and variability of the North Atlantic circulation: a perspective from ocean reanalyses. *J. Geophys. Res. Oceans* **124**, 9141–9170 (2019).
19. Lozier, M. S. et al. A sea change in our view of overturning in the subpolar North Atlantic. *Science* **363**, 516–521 (2019).
20. Li, F., Lozier, M. S. & Johns, W. Calculating the meridional volume, heat and freshwater transports from an observing system in the subpolar North Atlantic: observing system simulation experiment. *J. Atmos. Ocean. Technol.* https://doi.org/10.1175/JTECH-D-16-0247.1 (2017).
21. Desbruyères, D. G., Mercier, H., Maze, G. & Daniault, N. Surface predictor of overturning circulation and heat content change in the subpolar North Atlantic. *Ocean Sci.* **15**, 809–817 (2019).
22. Marshall, J. & Plumb, A. *Atmosphere, Ocean, and Climate Dynamics: An Introductory Text* (Elsevier, 2008).
23. Menary, M. B., Hermanson, L. & Dunstone, N. J. The impact of Labrador Sea temperature and salinity variability on density and the subpolar AMOC in a decadal prediction system. *Geophys. Res. Lett.* **43**, 12217–12227 (2016).
24. Zhao, J. & Johns, W. Wind-forced interannual variability of the Atlantic meridional overturning circulation at 26.5° N. *J. Geophys. Res. Oceans* **119**, 2403–2419 (2014).
25. Kanzow, T. et al. Seasonal variability of the Atlantic meridional overturning circulation at 26.5° N. *J. Clim.* **23**, 5678–5698 (2010).
26. Jones, D. C. et al. Local and remote influences on the heat content of the Labrador sea: an adjoint sensitivity study. *J. Geophys. Res. Oceans* **123**, 2646–2667 (2018).
27. Loose, N., Heimbach, P., Pillar, H. R. & Nisancioglu, K. H. Quantifying dynamical proxy potential through shared adjustment physics in the North Atlantic. *J. Geophys. Res. Oceans* **125**, e2020JC016112 (2020).
28. Fukumori, I., Wang, O., Llovel, W., Fenty, I. & Forget, G. A near-uniform fluctuation of ocean bottom pressure and sea level across the deep ocean basins of the Arctic Ocean and the Nordic Seas. *Progr. Oceanogr.* **134**, 152–172 (2015).
29. Eden, C. & Willebrand, J. Mechanism of interannual to decadal variability of the North Atlantic circulation. *J. Clim.* **14**, 2266–2280 (2001).
30. Getzlaff, J., Böning, C. W., Eden, C. & Biastoch, A. Signal propagation related to the North Atlantic overturning. *Geophys. Res. Lett.* **32**, L09602 (2005).
31. MacGilchrist, G. A. et al. Locations and mechanisms of ocean ventilation in the high-latitude North Atlantic in an eddy-permitting ocean model. *J. Clim.* https://doi.org/10.1175/JCLI-D-20-0191.1 (2020).
32. Zantopp, R., Fischer, J., Visbeck, M. & Karstensen, J. From interannual to decadal: 17 years of boundary current transports at the exit of the Labrador Sea. *J. Geophys. Res. Oceans* **122**, 1724–1748 (2017).
33. Zou, S., Lozier, M. S. & Buckley, M. How is meridional coherence maintained in the lower limb of the Atlantic meridional overturning circulation? *Geophys. Res. Lett.* **46**, 244–252 (2019).
34. Roemmich, D. et al. On the future of Argo: a global, full-depth, multi-disciplinary array. *Front. Mar. Sci.* **6**, 439 (2019).
35. McCarthy, G. D. et al. Measuring the Atlantic meridional overturning circulation at 26° N. *Prog. Oceanogr.* **130**, 91–111 (2015).

Methods

We use an algorithmic differentiation software, Transformation of Algorithms in FORTRAN (TAF[13]), to obtain the adjoint of the MITgcm in the ECCO version 4 configuration[14], whose release 3 covers the 1992–2015 period. The ECCO state estimate very skilfully reproduces the observed subtropical AMOC at the RAPID–MOCHA array. If we detrend and smooth the intermonthly time series with a 12-month running mean, the correlation between the state estimate and the RAPID–MOCHA observations is $R = 0.83$ (significant at the 1% level). In terms of the low-frequency variability, the RAPID–MOCHA overturning represented in ECCO does not show the same 2004–2006 positive anomaly as in the direct observational estimate. Hence, ECCO underestimates the subsequent decline at RAPID–MOCHA after 2006. Furthermore, towards the end of the observational record, there is a mismatch in the high-frequency variability between ECCO and RAPID–MOCHA observations despite the good agreement overall. The OSNAP observational record is too short to compute correlations with the ECCO historical state estimate. However, the ECCO time series mostly agree with the direct observational estimate at OSNAP-EAST within the observational uncertainty.

In this study, we modify the adjoint code of the MITgcm ECCO configuration and set up numerical calculations that output sensitivity patterns for the response of the Atlantic overturning to SST and SSS, as well as the response to surface wind stress assuming constant SST and SSS, at different lead times. Our objective functions for each adjoint calculation are defined in terms of volume transport in Sverdrups ($1\,\mathrm{Sv} = 10^6\,\mathrm{m^3\,s^{-1}}$).

We compute seasonal sensitivity patterns of the February, May, August and November monthly averaged overturning and for computational efficiency assume these to be representative of the winter, spring, summer and fall objective functions, respectively. This simplification introduces an annually cyclic bias in the buoyancy-related components of our reconstruction (see the apparent small oscillation in Fig. 3). Nevertheless, it is clear that the oscillations that arise due to this computational choice are small and with nearly compensating effects in the SST and SSS components. Hence, this does not affect our conclusions.

We perform two sets of adjoint calculations, each yielding the seasonally dependent linear sensitivity of the overturning at two different regions in the North Atlantic. First, we perform a set of calculations that give us the lagged sensitivity of the AMOC volume transport at 26° N in depth space to surface anomalies at different lead times and horizontal locations. Calculations for the AMOC strength at 26° N in potential density space give similar sensitivity results. Second, we perform an analogous set of calculations for the lagged sensitivity of the density-space overturning across the OSNAP-EAST line. To be consistent with observational products from the OSNAP array, we use potential density coordinates, referenced to the surface. The Eulerian velocity components at the vertical walls of each model grid cell are binned into different layers depending on the potential density interpolated onto the cell boundaries. We then obtain the OSNAP-EAST overturning by integrating the velocity across the array vertically, going from denser to lighter layers.

The sensitivity patterns we obtain depend on the time-evolving ocean state about which we linearize the model. To assess this nonlinear effect, we compute each set of sensitivity patterns twice, linearizing about two different periods of the ECCO state estimate: one ending in 2001–2002 and one in 2006–2007. We select these two representative periods, ending 10 and 15 years into the ECCO run, because the earlier years of the state estimate are marked by unusually strong convection in the subpolar North Atlantic. Computational cost limits our ability to repeat the adjoint calculation over additional periods. We consider both the mean and the spread between the two estimates and use each to reconstruct the AMOC time series and to identify sources of variability in Atlantic overturning. Figures 3 and 4 show sources of variability in the AMOC on the basis of a linearization of the model over the historical period ending in 2006–2007. By comparison, Supplementary Fig. 2 presents an analogous estimate but using a linearization over the earlier period ending in 2001–2002. When computing correlations, we use the mean of the two reconstructions.

In our reconstructions, we consider sensitivity to SST and SSS, rather than fluxes of heat and freshwater across the air–sea interface, because the former are more readily constrained by available in situ and satellite observations of the ocean. Moreover, air–sea fluxes are a step further removed from surface buoyancy compared with temperature and salinity. The ocean integrates local and remote surface fluxes, which then gives rise to SST and SSS anomalies. Therefore, if we used AMOC sensitivity to surface fluxes, we would have to consider much longer lead times, at which the adjoint of the MITgcm becomes less reliable (see a discussion in refs. [12,36]). For example, we would need accurate sensitivity to surface fluxes all along the Gulf Stream and the North Atlantic Current advective pathways going back years (Extended Data Fig. 4).

We convolve the sensitivity patterns from each set of adjoint calculations with 1992–2015 historical estimates of wind stress, SST and SSS anomalies from the ECCO ocean state estimate. We define anomalies in these fields relative to the climatological seasonal cycle. However, when exploring the wind contribution to AMOC variability (Fig. 2c,d), we also separately consider the impact of the climatological seasonal cycle in surface wind stress. Each convolution gives us an estimate for the time-evolving contribution $C_{\mathcal{P}}$ of a given ocean surface field $\mathcal{P}$ to historical variability in the rate of overturning:

$$C_{\mathcal{P}}(t) = \int_{t-\tau}^{t} \int \mathcal{P}(\mathbf{x}, t')\, \mathcal{G}_{\mathcal{P}}(t; \mathbf{x}, t - t')\, \mathrm{d}\mathbf{x}\, \mathrm{d}t' \qquad (3)$$

where $\mathcal{P}$ is the surface field anomaly relative to the climatological monthly mean. The function $\mathcal{G}_{\mathcal{P}}$ denotes the sensitivity pattern that depends on the season at time t, the lead time t' and the geographical location $\mathbf{x}$. To remove numerical noise, the patterns of sensitivity to SST and SSS are smoothed using a diffusive Gaussian operator[36,37] with a spatial decorrelation scale of two grid cells. This operator is not applied to wind stress sensitivity patterns, vector fields on an irregular model grid. The integration in space $\mathbf{x}$ is over the whole global ocean surface, and the time integration goes back to a cut-off lead time τ representing the assumed maximum memory of the AMOC to past forcing. The cut-off lead times are as follows: 3 years for wind stress in OSNAP-EAST reconstructions, 2 years for SST and SSS in OSNAP-EAST reconstructions and 6 years for all components in RAPID–AMOC reconstructions. In reality, the ocean circulation retains memory of previous forcing on much longer timescales. However, nonlinear effects are larger at longer lead times, and the adjoint of the MITgcm cannot capture them (see a discussion in refs. [12,36]). By sweeping parameter space in t', we have established that when we increase the cut-off lead times beyond the appropriate ranges we identify, our reconstruction skill decreases. This is likely due to the growth of nonlinear error terms at longer lead times. However, cut-off lead times that are unnecessarily short lead to omission of useful information about past forcing.

When computing the contributions due to wind stress, we use AMOC sensitivity patterns representative of 5-day steps in lead time. We convolve these sensitivity patterns with 5-day mean wind stress fields from ECCO. When estimating the contributions due to surface buoyancy, we use 10-day means for the SST, the SSS and the corresponding sensitivity patterns averaged over 10-day lead-time windows. Even though the ECCO configuration is nominally at a 1°×1° horizontal resolution, we need this submonthly temporal resolution because of the high-frequency, spatially localized winter convective variability in the subpolar North Atlantic. Summing the contributions due to wind stress, SST and SSS anomalies provides a partial reconstruction of the historical variability in the Atlantic overturning circulation relative to the seasonal cycle. Finally, we combine our reconstruction with the 1992–2015 climatological seasonal cycle in Atlantic overturning on the basis of the ECCO state estimate. Note that the OSNAP-EAST observational record is too short to estimate the background seasonal climatology in overturning. Furthermore, analysis of the OSNAP-EAST time series in ECCO suggests that variability relative to the seasonal cycle is comparable in amplitude to the seasonal cycle in subpolar overturning.

In this study, we identify the regions where variability in wind stress, SST and SSS most strongly projects on the corresponding AMOC sensitivity patterns and activates them. We consider the root-mean-square contribution per unit area ($\mathrm{Sv\,m^{-2}}$) to the convolutions in equation (1) over the period 1992–2015:

$$C_{\mathcal{P}}(\mathbf{x}) = \frac{1}{A(\mathbf{x})} \sqrt{\frac{1}{(T_f \cdot \tau)} \sum_{t=0}^{T_f} \sum_{t'=\max(t-\tau,0)}^{t} [\mathcal{P}(\mathbf{x}, t')\, \mathcal{G}_{\mathcal{P}}(t; \mathbf{x}, t - t')]^2} \qquad (4)$$

where $A(\mathbf{x})$ is the horizontal surface area of the model grid cell in location $\mathbf{x}$, $\mathcal{P}$ represents the surface field anomalies relative to the climatology at a lead time t' summed up to a finite maximum memory τ, as in equation (3). The function $\mathcal{G}_{\mathcal{P}}$ is the corresponding sensitivity pattern that depends on the season, as in equation (3). We sum the convolution of $\mathcal{P}$ and $\mathcal{G}_{\mathcal{P}}$ until the end of the available time series $t = T_f$ and compute the root mean square.

We acknowledge that the AMOC sensitivity patterns, reconstructions and attributions presented here are based on a model that approximates processes in the ocean. For example, the regions of deep winter convection in the North Atlantic are known to differ widely across climate models[38]. Moreover, the ECCO configuration of the MITgcm that we use does not resolve mesoscale ocean eddies, whose important role in the circulation is instead represented via a widely used parameterization. Nevertheless, since ECCO formally calibrates the spatially varying parameters in the model's eddy transport scheme using observational constraints[10], the evolving state of the ocean in ECCO closely tracks historical temperature, salinity and ocean circulation conditions[16].

We compare our model-based results with observational data from the RAPID–MOCHA array at 26° N and the OSNAP arrays in the subpolar North Atlantic.

In the subpolar latitudes, recent and pre-existing OSNAP moorings on the basin boundaries measure temperature, salinity, density and velocity[5,32]. Away from the OSNAP moorings, an objective analysis method is used to interpolate between these measurements using data from Argo profiles (for example, ref. [39]) and OSNAP gliders, as well as World Ocean Atlas 2013 climatology[40]. In addition, away from the arrays, Ekman velocities are estimated from European Centre for Medium-Range Weather Forecasts European Reanalysis-Interim wind fields[41]. This wind-driven ageostrophic transport is assumed to be confined to the Ekman surface boundary layer[22]. Geostrophic velocity[22] is estimated using two different reference velocities. Wherever deep moorings are available, their velocity measurements are used as a reference, except in the western Labrador Sea

and the central Iceland Basin. Otherwise, time-mean surface velocity data from satellite altimetry provides the reference velocity. Finally, to guarantee a zero net mass transport across the entire OSNAP array, a compensation transport term is included at OSNAP-WEST at each time step. The same term is added with the opposite sign across OSNAP-EAST. These compensation terms are distributed uniformly in regions where velocity measurements are not available.

We furthermore use publicly available observational data for the subtropical AMOC provided by the RAPID project[4,35]. We bin the RAPID–MOCHA overturning time series into the same 30-day windows as our model output and reconstructions.

When comparing time series from the state estimate, reconstructions and observations, we compute correlation coefficients using standard methods for linear regression. When we test the significance of the regression coefficients, we consider the redness in the spectral properties of the time series. Thus, our null hypothesis is not based on a standard normal distribution. Instead, we use an established spectral Monte Carlo approach for significance testing[42,43]. All regression coefficients cited in this study are significant at the 1% level.

Data availability

The OSNAP data products are publicly available at www.o-snap.org. The derived data including the OSNAP-EAST overturning are furthermore available in Duke Digital Repository, https://research.repository.duke.edu/collections/1z40kt318. The RAPID–MOCHA overturning time series is available at https://www.rapid.ac.uk/rapidmoc/rapid_data/datadl.php.

Code availability

The code for the MITgcm and the scripts for post-processing model output are available at https://github.com/MITgcm/. The ECCO state estimate model configuration can be downloaded from https://github.com/gaelforget/ECCOv4, with initial and boundary conditions available at https://web.corral.tacc.utexas.edu/OceanProjects/ECCO/ECCOv4. The TAF algorithmic differentiation software is proprietary and provided by FastOpt. Code used to process data and produce figures is available from the corresponding author upon reasonable request.

References

36. Kostov, Y., Johnson, H. L. & Marshall, D. P. AMOC sensitivity to surface buoyancy fluxes: the role of air–sea feedback mechanisms. *Clim. Dyn.* **53**, 4521–4537 (2019).
37. Weaver, A. T. & Courtier, P. Correlation modelling on the sphere using a generalized diffusion equation. *Q. J. R. Meteorol. Soc.* **127**, 1815–1846 (2001).
38. Heuzé, C. North Atlantic deep water formation and AMOC in CMIP5 models. *Ocean Sci.* **13**, 609–622 (2017).
39. Forget, G., Mercier, H. & Ferron, B. Combining Argo profiles with a general circulation model in the North Atlantic. Part 2: realistic transports and improved hydrography, between spring 2002 and spring 2003. *Ocean Model.* **20**, 17–34 (2008).
40. Locarnini, R. A. et al. in *World Ocean Atlas 2009: Temperature. NOAA Atlas NESDIS 68* Vol. 1 (ed. Levitus, S.) 184 (US Government Printing Office 2010).
41. Dee, D. P. et al. The ERA-Interim reanalysis: configuration and performance of the data assimilation system. *Q. J. R. Meteorol. Soc.* **137**, 553–597 (2011).
42. Lund, I. A. A Monte Carlo method for testing the statistical significance of a regression equation. *J. Appl. Meteor.* **9**, 330–332 (1970).
43. Cornish, S. B., Kostov, Y., Johnson, H. L. & Lique, C. Response of Arctic freshwater to the Arctic oscillation in coupled climate models. *J. Clim.* **33**, 2533–2555 (2020).

Acknowledgements

This study used the ARCHER UK National Supercomputing Service (http://www.archer.ac.uk). In our analysis, we apply the TAF software provided by FastOpt. The maps used in the figures and supplementary material were produced using the freely available software M_Map: A mapping package for MATLAB, provided by R. Pawlowicz. We thank the groups that maintain the OSNAP and RAPID–MOCHA observational networks and the developers of the ECCO version 4 state estimate. Y.K. was funded by the OSNAP project through NERC grant NE/K010948/1 and the TICTOC project through NERC grant NE/P019064/1. H.L.J. and D.P.M. were also funded by NERC grant NE/K010948/1. G.F. acknowledges support from NASA award no. 6937342 and the Simons Foundation award no. 549931. P.H., H.R.P. and T.S. were supported in part by NOAA grant NOAA/NA130AR4310135, NSF grant NSF-OCE-1924546 and a JPL/Caltech subcontract. T.S. received additional funding from an Oden Institute CSEM fellowship. N.P.H. was funded by the OSNAP NERC grant NE/K010875/1. M.S.L. and F.L. were supported by NSF grants OCE-1948335 and OCE-1924456.

Author contributions

All authors discussed the results and contributed to the preparation of the final manuscript. Y.K. took the lead in writing the text while holding regular discussions with H.L.J., D.P.M., T.S. and H.R.P. Y.K. planned, designed and performed the adjoint sensitivity analysis with the MITgcm. P.H. and G.F. developed and maintained the ECCO version 4 state estimate and the associated tools for post-processing MITgcm output on an irregular grid. T.S. adapted the MITgcm diagnostic package. N.P.H., F.L. and M.S.L. developed and applied the data analysis methodology for OSNAP observations, and F.L. provided the OSNAP-EAST overturning time series.

Competing interests

The authors declare no competing interests.

Additional information

Extended data is available for this paper at https://doi.org/10.1038/s41561-021-00759-4.

Supplementary information The online version contains supplementary material available at https://doi.org/10.1038/s41561-021-00759-4.

Correspondence and requests for materials should be addressed to Y.K.

Peer review information *Nature Geoscience* thanks the anonymous reviewers for their contribution to the peer review of this work. Primary Handling Editor: James Super.

Reprints and permissions information is available at www.nature.com/reprints.

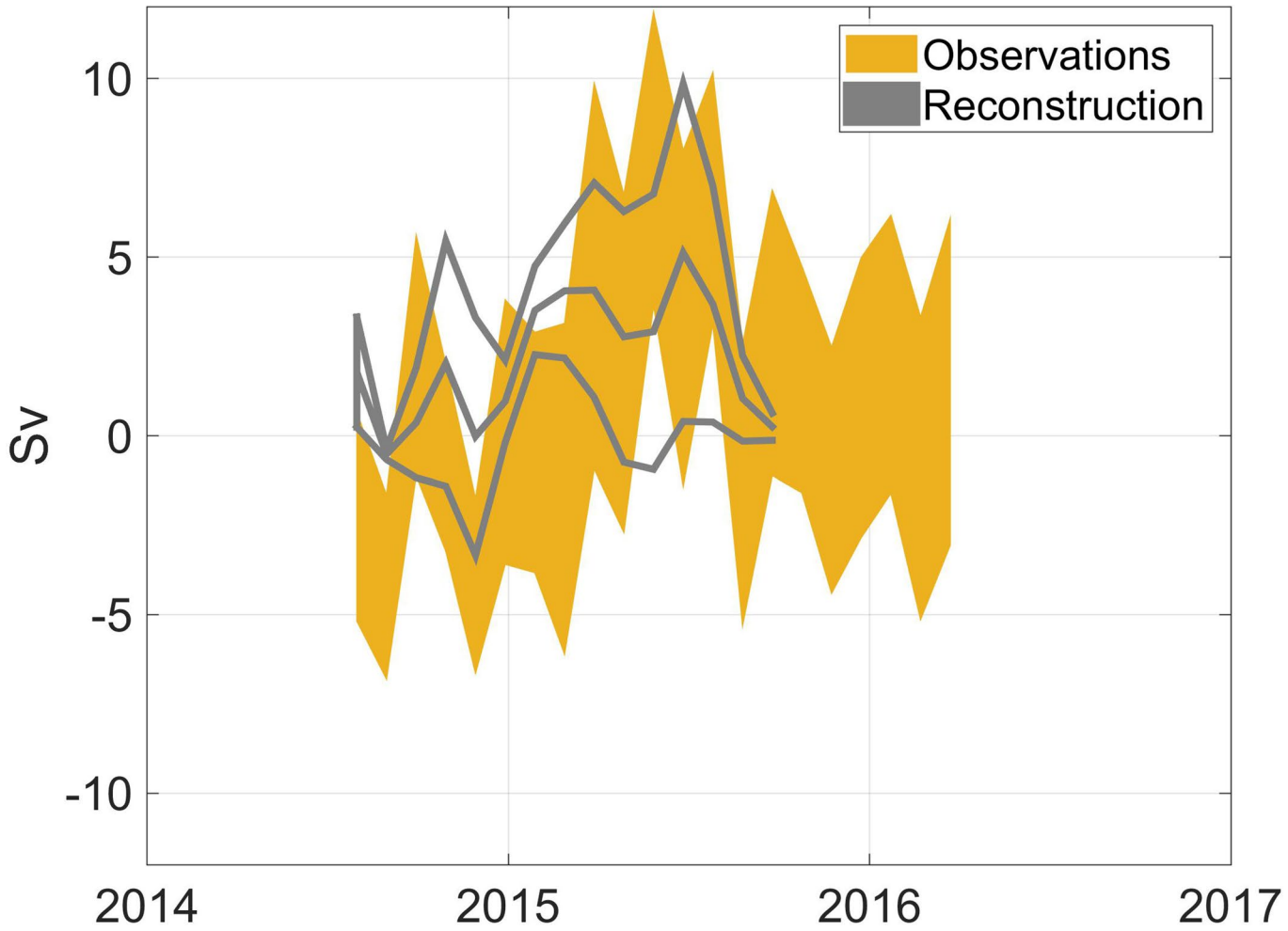

Extended Data Fig. 1 | Reconstruction skill for OSNAP-EAST observations. Comparison between observations (yellow envelope showing ±1 standard deviation of the observational uncertainty) and our two reconstructions (outer gray contours) of OSNAP-EAST overturning [Sv] based on two different sets of sensitivity patterns: one set from objective functions in 2001–2002, and a second set from objective functions in 2006–2007. The reconstructions are interpolated onto the same 30-day windows as the observations. We consider both the mean of our two reconstructions (middle gray contour) and the spread between them (outer gray contours). Note that our reconstruction estimate uses the ECCOv4r3 mean seasonal cycle, since the observational record at OSNAP-EAST is short.

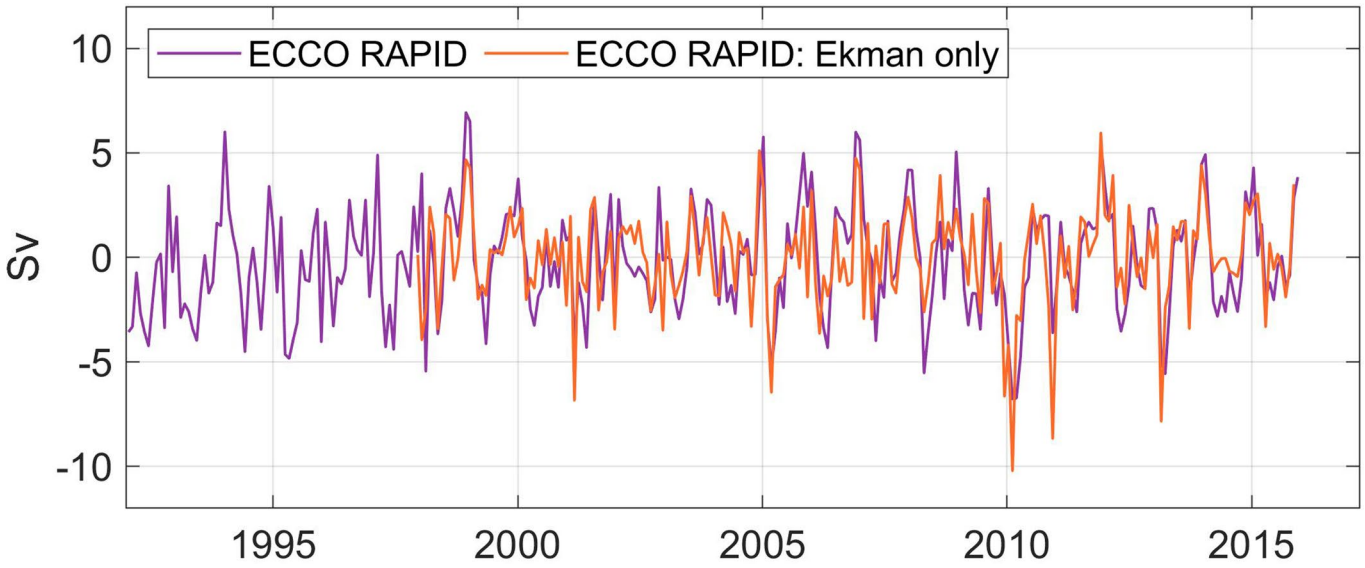

Extended Data Fig. 2 | Ekman transport contribution to overturning variability at RAPID-MOCHA in ECCO. ECCO-based comparison between variability in RAPID-MOCHA overturning (purple) and Ekman transport variability at 26°N (orange) over the time-period of the linear reconstructions in the main text. Anomalies are shown relative to the long-term mean.

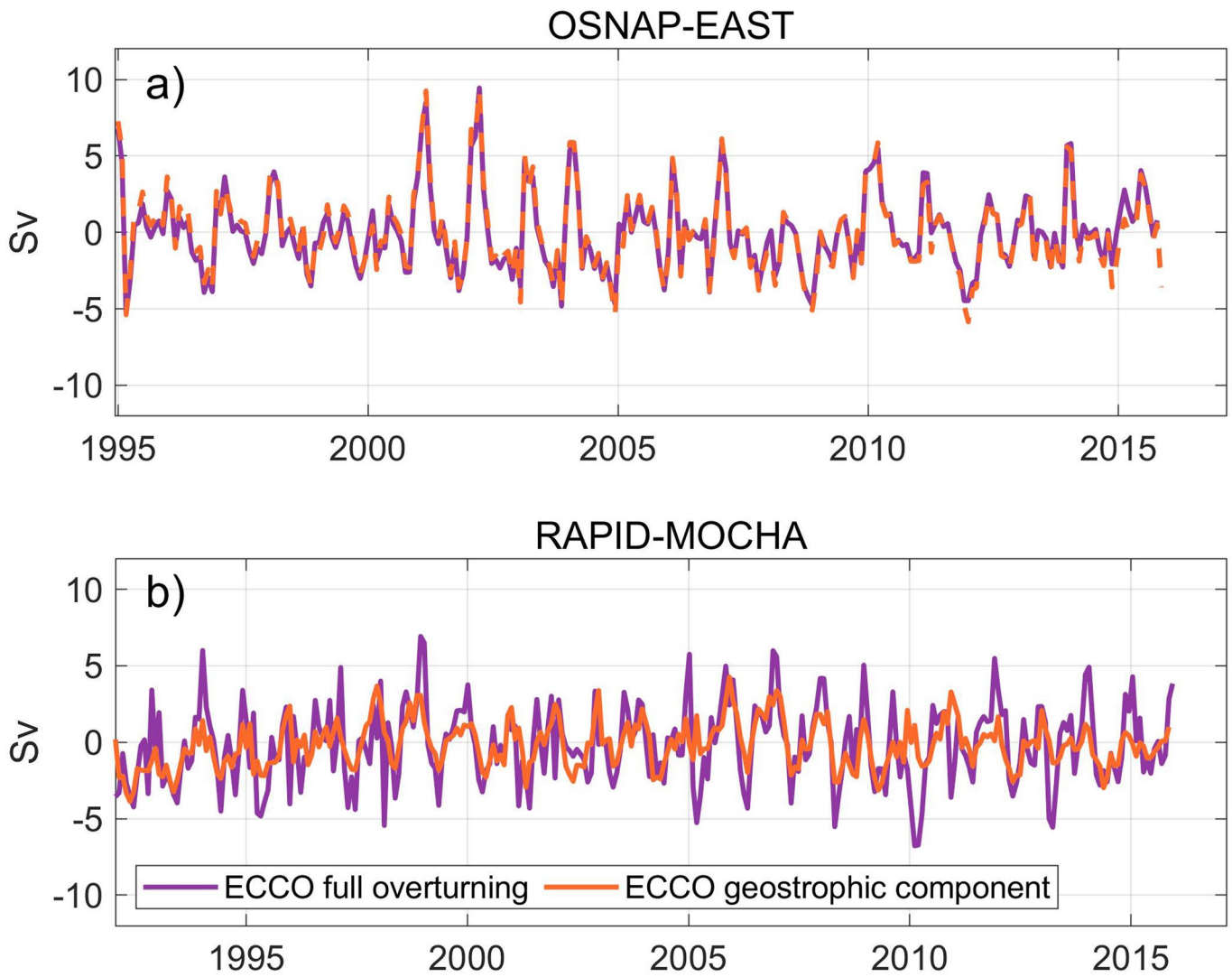

Extended Data Fig. 3 | Geostrophic component of overturning in the North Atlantic. Overturning variability (purple, volume transport in Sv) at OSNAP-EAST (**a**) and RAPID-MOCHA (**b**) in the ECCO state estimate contrasted against variability in the geostrophic component of overturning (orange). The comparison in **a** spans the time-period of the linear reconstructions in the main text. Anomalies are shown relative to the long-term mean.

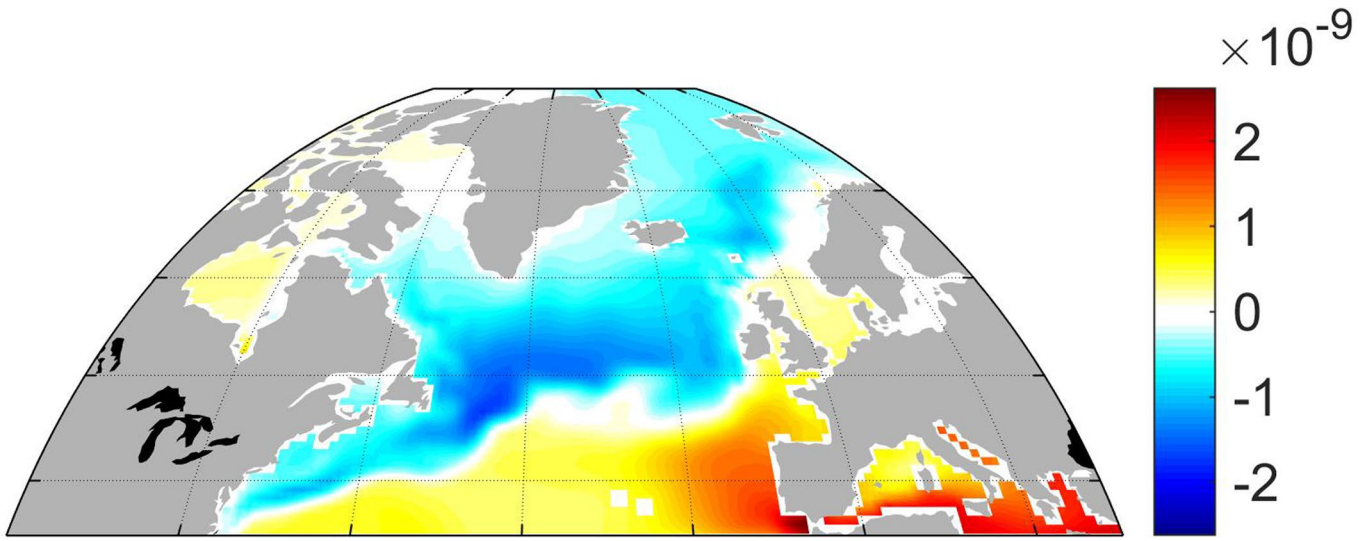

Extended Data Fig. 4 | Sensitivity of the OSNAP-EAST overturning to surface heat fluxes. Sensitivity of the OSNAP-EAST overturning in February 2007 to net surface heat fluxes [Sv per (W m^{-2} sustained over 1 hour)] at a lead time of nine years. Red shading indicates that heat flux into the ocean contributes to a delayed strengthening of the OSNAP-EAST overturning 9 years later. Blue shading indicates that cooling the ocean surface at that lead time causes a lagged strengthening of the OSNAP-EAST overturning. Notice the pattern tracking the Gulf Stream – North Atlantic Current advective pathway from the Caribbean to the subpolar latitudes. This *long memory* of past sea surface fluxes motivates the use of AMOC sensitivity to SST and SSS instead.

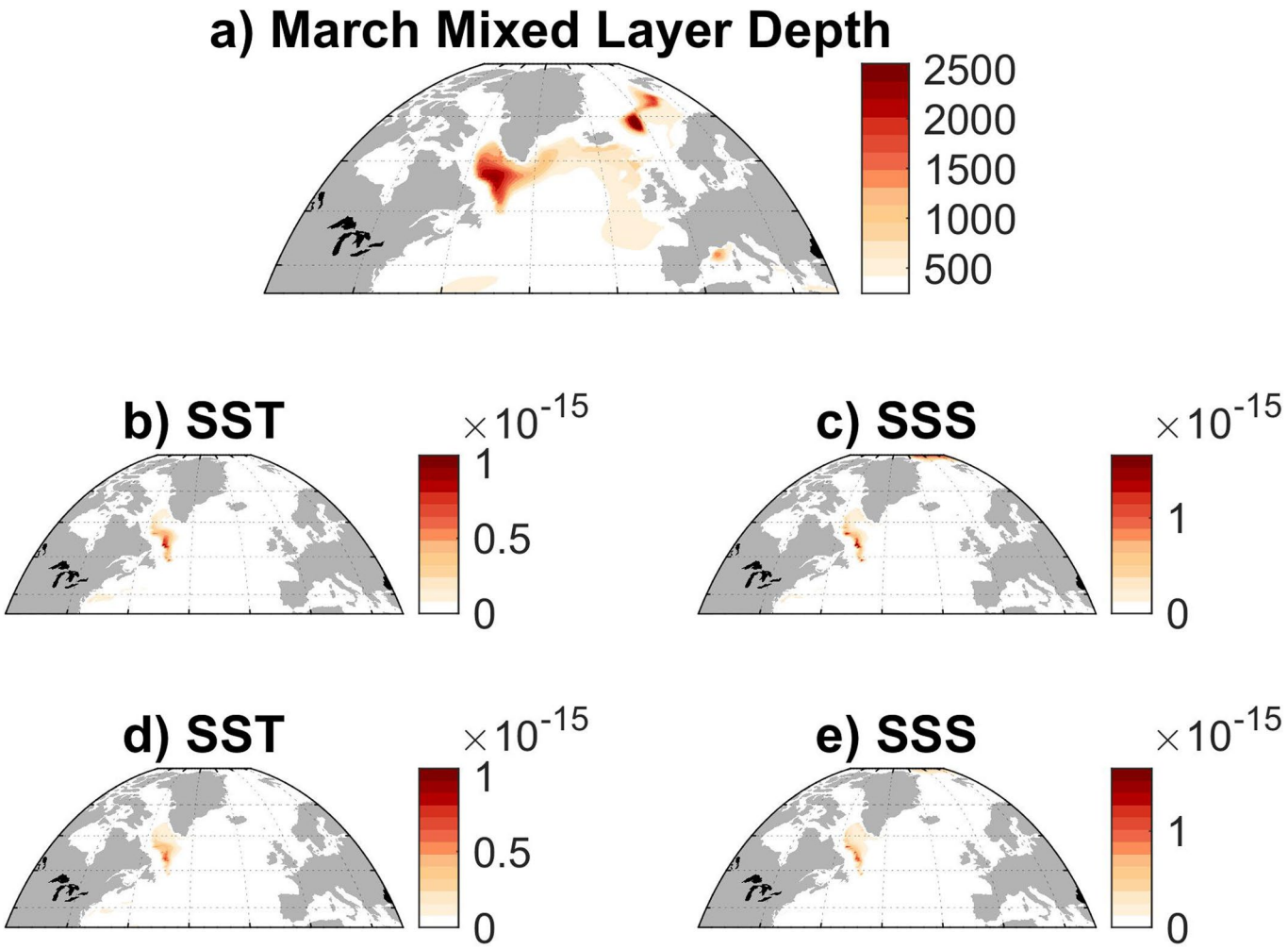

Extended Data Fig. 5 | North Atlantic mixed layer depth and spatial origins of buoyancy-driven variability in RAPID-MOCHA overturning. a, Climatological March mixed layer depth [m] in ECCO; **b–e**, Spatial sources of variability in the RAPID-MOCHA AMOC overturning: root-mean-square contribution per unit area [Sv m^{-2}] to the convolutions in equation(1) of the main text over the period 1992–2015 using sensitivity patterns based on (**b**,**c**) 2006–2007 and (**d**,**e**) 2001–2002 AMOC objective functions. Contributions due to SST (**b**,**d**), and SSS (**c**,**e**) all relative to the seasonal cycle. The scale in all panels is linear.